Research Article

Journal of Algorithms & Computational Technology

Journal of Algorithms & Computational Technology
0(0) 1–15

DOI: 10.1177/1748301816665527
act.sagepub.com

SAGE

Computational methods for investigation of surface curvature effects on airfoil boundary layer behavior

Xiang Shen[1], Eldad Avital[1], Mohammad Amin Rezaienia[1], Gordon Paul[1] and Theodosios Korakianitis[2]

Abstract

This article presents computational algorithms for the design, analysis, and optimization of airfoil aerodynamic performance. The prescribed surface curvature distribution blade design (CIRCLE) method is applied to a symmetrical airfoil NACA0012 and a non-symmetrical airfoil E387 to remove their surface curvature and slope-of-curvature discontinuities. Computational fluid dynamics analysis is used to investigate the effects of curvature distribution on aerodynamic performance of the original and modified airfoils. An inviscid–viscid interaction scheme is introduced to predict the positions of laminar separation bubbles. The results are compared with experimental data obtained from tests on the original airfoil geometry. The computed aerodynamic advantages of the modified airfoils are analyzed in different operating conditions. The leading edge singularity of NACA0012 is removed and it is shown that the surface curvature discontinuity affects aerodynamic performance near the stalling angle of attack. The discontinuous slope-of-curvature distribution of E387 results in a larger laminar separation bubble at lower angles of attack and lower Reynolds numbers. It also affects the inherent performance of the airfoil at higher Reynolds numbers. It is shown that at relatively high angles of attack, a continuous slope-of-curvature distribution reduces the skin friction by suppressing both laminar and turbulent separation, and by delaying laminar-turbulent transition. It is concluded that the surface curvature distribution has significant effects on the boundary layer behavior and consequently an improved curvature distribution will lead to higher aerodynamic efficiency.

Keywords

Thin airfoil theory, surface curvature, boundary layer, aerodynamic efficiency

Date received: 13 October 2015; accepted: 31 March 2016

Introduction

As the basic element of wings or blades, airfoils are geometric profiles that are designed to generate lift force due to a relative motion in a fluid. Their aerodynamic performance directly determines the overall performance and efficiency of a system. Therefore, airfoil design plays a key role in an aeronautical device design. Early design methods were based on specifying a thickness distribution around a camber line.[1] These methods did not provide enough flexibility to control both the suction and pressure surfaces to obtain a desirable aerodynamic performance. Modern designers use different definitions for airfoil and blade design methods: direct design,[2] semi-inverse design,[3] full-inverse design,[4] or full- optimization methods.[5] The analysis of aerodynamic performance can be studied by several methods, including Conformal Mapping,[6] Thin Airfoil Theory,[7] Surface Panel Method,[8] or computational fluid dynamics (CFD) solutions.[9,10]

The working airflow moves over an airfoil along the surface curves, rather than Cartesian coordinates. When the boundary layer equations are written in curvilinear coordinates, the equations show that local pressure on an airfoil surface has a strong dependence

[1]School of Engineering and Materials Science, Queen Mary University of London, London, UK
[2]Parks College of Engineering, Aviation and Technology, Saint Louis University, St. Louis, USA

Corresponding author:
Theodosios Korakianitis, Parks College of Engineering, Aviation and Technology, Saint Louis University, St. Louis, MO 63103, USA.
Email: korakianitis@alum.mit.edu

on local radius of curvature.[11] Local curvature is determined by the radius of local curvature, which is directly related to the second-order derivative of local surface equation y''. The importance of y'' for aerodynamic performance can also be found in the thin airfoil theory. Van Dyke[7] presented the second-order extension of thin airfoil theory showing that the surface pressure and velocity distributions are strongly dependent on the second-order derivative of the airfoil surface function y. Thus, smooth velocity and pressure distributions along the airfoil surface require smooth second-order derivative of the airfoil surface function, and hence smooth surface curvature distributions (i.e. continuous slope-of-curvature distributions) along the surface. A continuous slope-of-curvature requires a continuous third-order derivative of the surface function.

One must distinguish between ''smooth surface'' and ''smooth curvature distribution'' as these terms are often confused in the literature. When we say an airfoil has a smooth surface, mathematically it means that the first-order derivative of surface function y' is continuous, not the second or third order. However, smooth curvature distribution means that it has a continuous slope-of-curvature distribution, which requires that the third-order derivative of the surface function is continuous. In this article, we deal with the latter concept and we address ''smooth curvature distribution'' as ''continuous slope-of-curvature distribution'' in order to be consistent. Surface curvature discontinuity often exists at particular areas on airfoils such as the leading edge (LE), e.g. NACA four-digit airfoils, or the trailing edge (TE), e.g. non-symmetrical sharp or blunt TE airfoils. Many blades and airfoils present slope-of-curvature discontinuities, at the point where the LE circle or other shape joins the main part of the airfoil. Whether discontinuity of slope-of-curvature is present depends on the airfoil design methods and airfoil coordinates resources. The discontinuities in the distribution of surface curvature and slope-of-curvature are invisible to the observer in the airfoil shapes and the airfoil surfaces can appear to be smooth. However, the airfoils with these discontinuities often produce unusual loads, higher losses, and thicker wakes.[12]

To eliminate unnecessary local changes of surface curvature, surface curvature distribution becomes one of the key factors in the design of high-efficiency airfoils and blades.[13–15] Siddappaji et al.[16] developed a parametric 3D blade design tool for turbomachinery, and they used the definition of splines to modify the blade shapes and obtain the desired blade model. In their research, the curvature as well as the slope-of-curvature distributions of the blade surface are both continuous due to the application of the splines. This design tool was later improved by Nemnem et al.[17] by the addition of a 2D curvature-defined mean-line blade airfoil geometry generator. They created a fifth-order mean-line by twice integrating the cubic B-spline, which ensures curvature and slope-of-curvature distributions are continuous, and improved the performance of newly designed blades. A design method called the prescribed surface curvature distribution blade design (CIRCLE) method[18] was proposed to optimize airfoils and blades by ensuring continuous curvature and slope-of-curvature distribution along their surfaces, and showed that the aerodynamic and heat transfer performance strongly depends on surface curvature distribution. Massardo et al.[19,20] used streamline curvature distribution calculations to determine the 3D variation of inlet and outlet flow angles for axial-flow compressor design and improved the compressor efficiency. Based on surface curvature distribution, Song et al.[13,21] showed that improving the curvature continuity at the leading-edge blend point of a compressor blade improved performance by helping to eliminate the separation bubble. They also proved that the main surface curvature continuity improves blade performance. Korakianitis et al.[22] applied the CIRCLE method to two wind turbine airfoils and concluded that more continuous surface curvature and slope-of-curvature distributions improved the aerodynamic performance compared with the original wind turbine airfoils.

Although the effects of surface curvature discontinuities are widely researched in turbomachinery blade and airfoil design, more research attention is required to examine the impact of surface curvature distribution on the behavior of the airfoil boundary layer in external aerodynamics applications. At low Reynolds numbers, the flow on airfoils separates due to a sufficiently large magnitude of the adverse pressure gradient and changes in flow geometry including local surface curvature variations. The flow experiences transition to turbulence and can result in a stall (without turbulent re-attachment) or a laminar separation bubble (LSB; with turbulent re-attachment).[23] Subjected to inherent effects of flow separation and stall, the airfoils operating at low Reynolds numbers do not always offer good aerodynamic performance.[24] Therefore, more research is needed on the aerodynamic mechanisms causing the improved performance yielded by airfoils with continuous slope-of-curvature distributions.

In this study, the CIRCLE method[25] is used to redesign airfoils by removing their surface curvature and slope of surface curvature discontinuities from LE to TE. A symmetrical airfoil NACA0012 and a non-symmetrical airfoil E387 are judiciously selected for this investigation due to the existence of discontinuities of curvature and slope-of-curvature, their widespread use and the availability of detailed experimental measurements of airfoil performance.[27,28] NACA 0012 is used

as an example of an airfoil with a surface curvature discontinuity and E387 is used as an example of an airfoil with slope-of-curvature discontinuities. Reynolds Averaged Navier–Stokes (RANS) computations are applied to both airfoils to numerically investigate the effects of surface curvature on boundary layer behavior, which significantly affects airfoil aerodynamic performance. An inviscid–viscid interaction flow computing scheme of thin airfoil theory and boundary layer models named TATO is used to calculate the external flow velocity and LSB characteristics of the original E387 and the airfoil optimized with the CIRCLE method. The flowchart of this study is presented in Figure 1.

Methodology

Design approach: The CIRCLE method

In this section, the CIRCLE method for the section side of an airfoil is summarized, and the design procedure for the pressure side of the airfoil is similar.[25] Curvature *Curv* and slope-of-curvature *Curv′* are defined as follows:

$$Curv = \frac{1}{r} = \frac{y''}{(1+y'2)^{3/2}} \tag{1}$$

$$Curv' = \frac{d(Curv)}{dx} = \frac{y'''(1+y'2) - 3y'y''2}{(1+y'2)^{5/2}} \tag{2}$$

where r denotes radius of curvature, (x, y) denotes Cartesian coordinates and y', y'', y''' are the first-, second-, and third-order derivative of y. The sign of the curvature is usually defined as the direction of the unit tangent vector moving along the curve. We define curvature as positive if the vector rotates clockwise, otherwise it is negative. As described in the equation, the sign of the curvature is always the same as the sign of the second derivative of airfoil surface function y''.

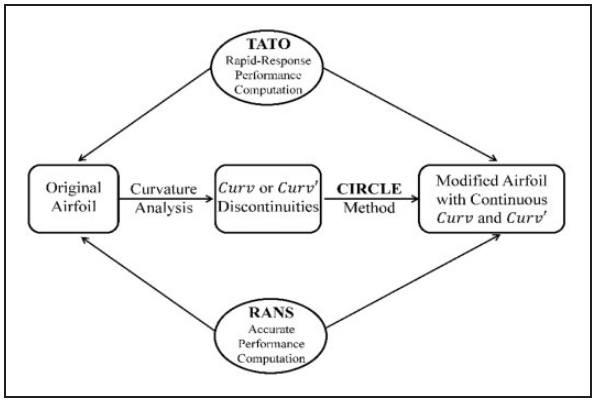

Figure 1. The main flow chart for the design and computation algorithms in this study. *Curv* and *Curv′* represents curvature and slope-of-curvature, respectively.

Circular geometry is used for LE and TE design to illustrate the design process, yet in principle, any proper geometry (e.g. ellipse) with a continuous slope-of-curvature distribution can be used to design. The CIRCLE method starts from the TE circle and designs the airfoil shape in three line segments sequentially: *y3* near the TE (treated as a small circle in this section), *y2* in the middle part of the surface, *y1* near the LE (also treated as a small circle in this section), and the LE circle, as shown in Figure 2(a). By specification, the method ensures that airfoil surface curvature and slope-of-curvature is continuous from the LE stagnation point to the TE stagnation point. This section describes the approaches for the design of the TE, main body, and LE.

TE design. The most difficult and complicated part of TE design is joining the TE circle to the airfoil surfaces, as there is a transition from the constant curvature of the circle region to the locally varying curvature of the remaining airfoil surface. The TE circle is located by the TE origin and its radius. On the suction side, the airfoil surface connects to the TE circle at point P_{s2}, as shown in Figure 2(b). The position of point P_{s2} is specified by the input parameter TE origin and its local airfoil surface angle β_{s2}. The line segment *y3* extends from point P_{s2} to P_{sm} as in Figure 2(a) and (b), and is specified by an analytic polynomial $y = f(x)$ of the exponential form:

$$\begin{aligned} y3 = f(x) &= c_0 + c_1 x + c_2 x^2 + c_3 x^3 \\ &+ c_4 k_1 [x - x(P_{s2})] + c_5 k_2 [x - x(P_{s2})] \end{aligned} \tag{3}$$

where k_1 and k_2 are exponential functions, c_0 to c_5 are thickness coefficients. k_1 and k_2 present increasing importance when approaching point P_{s2}. Thus, the equation can be considered as a cubic equation near point P_{sm}; and as exponential modifications of the basic cubic equation when it approaches the TE circle at point P_{s2}.

The six thickness coefficients c_0 to c_5 are evaluated from six conditional equations, which are the conditions of the point continuity, the first-, second-, and third-order derivative continuity (four conditions) of the airfoil surface line at P_{s2}, and prescribing the point and its first-order derivative continuity at P_{sm} (two additional conditions). As the TE circle is usually small, the variation in the streamwise curvature from the TE circle to the line segment *y3* is usually large. The CIRCLE method enforces curvature and slope-of-curvature continuity through these locally large streamwise changes of curvature.[18]

The circular (or elliptical) form of the TE is necessary. It guarantees the slope-of-curvature continuity

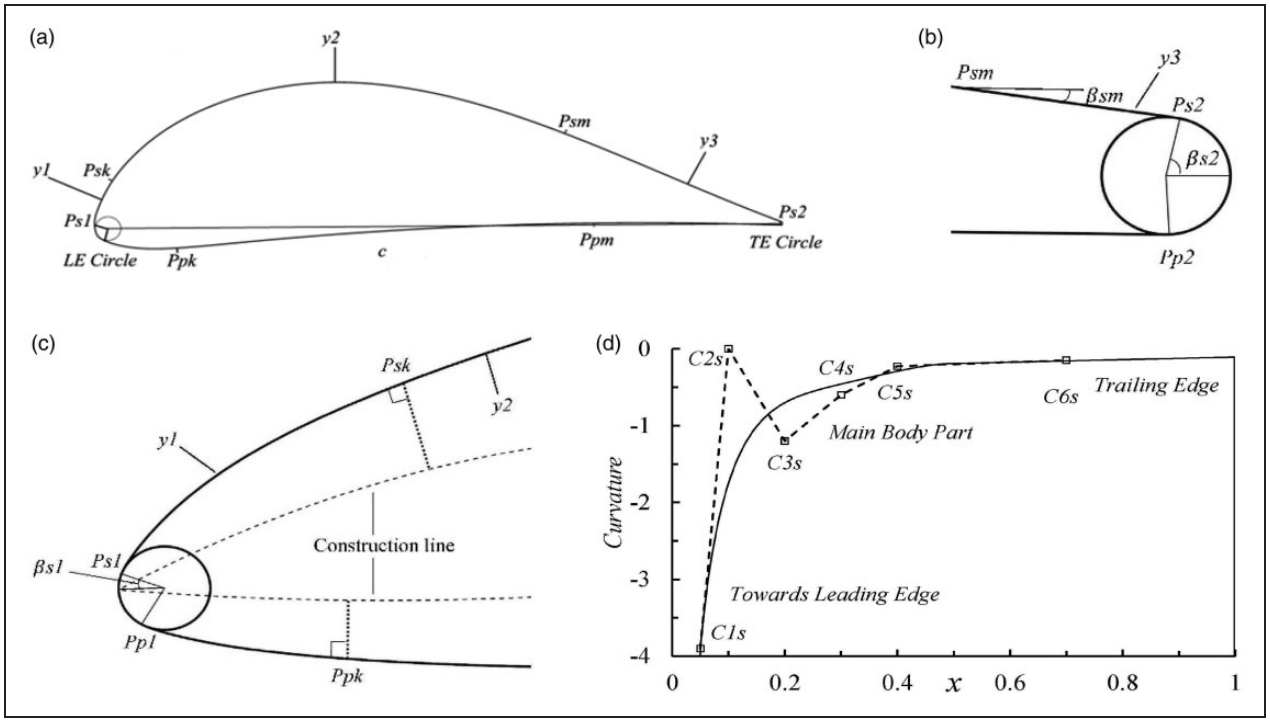

Figure 2. The CIRCLE method for an airfoil design: (a) Main blade geometry (adapted from Korakianitis et al.[26]); (b) trailing edge design; (c) leading edge design; (d) suction side surface prescribed curvature distribution.

near TE region, which provides smooth surface curvature distribution and therefore smooth pressure and velocity distribution, and also avoids a TE mathematical singularity (sharp TE) causing a bursting increase of the skin friction at the TE region, which will be described in the following sections. Moreover, it is easier to manufacture as compared with airfoils with a sharp TE as in reality, it is impossible to produce a zero thickness TE.

Main body design. Bezier splines are used to design the line segment *y2* between points P_{sm} and P_{sk}. *y2* is constructed by mapping the curvature distribution from the original airfoil geometry. The curvature segment from P_{s2} to P_{sm} is evaluated from the analytic polynomial *y3* (equation 3) starting from the TE and ending at point *C6s* in Figure 2(d). The slope of the curvature at point *C6s* is computed from equation (3) and becomes an input parameter to further calculations. Points *C1s* to *C5s* are user specified parameters. Point *C1s* is specified at an x location corresponding to the point P_{sk}. The tangency condition at point *C6s* ensures slope-of-curvature continuity from P_{sm} to P_{sk} because the slope of the Bezier curve is tangent to the line of both ends of the curve.

Starting from point P_{sm}, the design progresses explicitly point-by-point toward the LE to points P_{sk} and we obtain each y_{i+1} by using central differences equation for curvature at airfoil point i as a function of (x, y) coordinates of points $i-1$, i, and $i+1$. The Bezier spline is iteratively manipulated until the slope and the y location of the airfoil surface are achieved at points P_{sk}.[25]

LE design. The CIRCLE method used a hybrid method to design the LE region. The suction side surface connects the LE circle at point P_{s1}, which is specified by an input parameter LE local surface angle β_{s1}. Here, a parabolic construction line is defined and a thickness distribution is added perpendicularly to the construction line, as in Figure 2(c). The construction line starts from the LE of the airfoil, or the center of the LE circle. A thickness distribution is added orthogonally to this parabolic construction line, so that the thickness distribution has continuous point, first, second, and third derivative (continuous y, y', y'', y''' and therefore continuous $Curv'$) at both points P_{s1} and P_{sk}, as discussed below. Point P_{s1} is the point connecting the LE thickness distribution to the LE shape. Point P_{sk} is the point connecting resultant line *y1* (from the thickness distribution) to the main part of the airfoil *y2*, corresponding to curvature point *C1s*, as in Figure 2(d). The suction side construction line can be of the form: $y(x) = Ax^2 + Bx + C$, and the thickness distribution y_t can be expressed as:

$$y_t = c_0 + c_1 x + c_2 x^2 + c_3 x^3 + (c_4 k_{11} + c_6 k_{13}) \times [x - x(P_{s1})] + (c_5 k_{12} + c_7 k_{14})[x - x(P_{sk})] \quad (4)$$

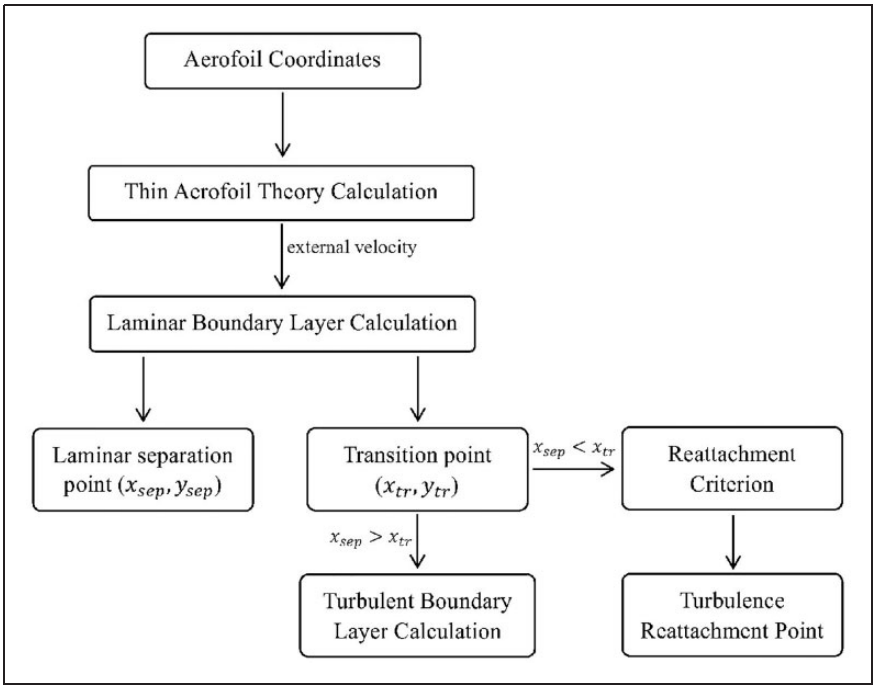

Figure 3. The program flow chart for Thin Airfoil Theory Code (TATO).

where functions k_{11}, k_{12}, k_{13}, and k_{14} are exponential polynomials, similar to k_1 and k_2 as explained in the subsection of TE design. These exponential functions have increasing importance when approaching the end points P_{s1} and P_{sk} of line segment $y1$. Equation (4) is a cubic polynomial away from these two end points. The eight parameters of the thickness function c_0 to c_7 need eight equations and they are derived from the conditions to match: y, y', y'', and y''' at point P_{s1} and at point P_{sk}, respectively. This approach ensures continuity of curvature and slope-of-curvature from the TE circle to the main part of the airfoil surface through the leading-edge thickness distribution and finally into the LE circle.

Computational methods

Two computational methods are used in this article. An inviscid–viscid interaction scheme called Thin Airfoil Theory cOde (TATO) is introduced as an engineering algorithm to calculate LSB positions. RANS computations are applied to simulate the flow field of the airfoils. The results of these two methods are compared in the results section.

TATO. An inviscid–viscid interaction scheme is adopted for the LSB and flow transition calculation. The inviscid solution is achieved by thin airfoil theory calculations, providing flow field information including the external velocity of the airfoil. Boundary layer calculations are carried out to determine boundary layer displacement effects, supplying separation, transition, and re-attachment states. The general procedural elements are presented in Figure 3.

Classical thin airfoil theory. The profile of the upper and lower surfaces of an airfoil can be described by the camber and thickness functions of the airfoil. A solution based on potential incompressible theory of thin airfoil of moderate thickness and camber at a moderate angle of attack was proposed by Van Dyke.[7] The inviscid external velocity q is determined by two horizontal velocity disturbances on the chord line assuming first- and second-order perturbations.

Boundary layer methods. Thwaites' method[29] is adopted to determine the location of the laminar separation point. Thwaites proposed a laminar separation parameter m:

$$m = -\frac{\theta^2}{\nu}\frac{dq}{dx} \tag{5}$$

where θ denotes boundary layer momentum thickness and ν denotes air kinematic viscosity. He suggested that the laminar flow is on the separation point when $m = 0.082$. It was later corrected to 0.09 by Curle and Skan.[30] Michel's empirical formula are used to

calculate the location of transition according to the momentum thickness of local boundary layer.[31] The formula suggests that transition happens when the Reynolds number based on the momentum thickness Re_θ meets the following equation:

$$Re_{\theta_{tr}} = 1.174(1 + \frac{22400}{Re_{x_{tr}}})Re_{x_{tr}}^{0.46} \quad (6)$$

where $Re_\theta = q\theta/\nu$, $Re_x = ql/\nu$ and l is the curve length between local position on airfoil surface and stagnation point as the reference length. If the separation point is before the transition point, a LSB forms. The turbulence re-attachment can be calculated with Horton's criterion[32] and Roberts' correction[33]:

$$\Lambda_R = \left(\frac{\theta}{q}\frac{dq}{dx}\right)_R = -0.0059 \quad (7)$$

where Λ_R is a re-attachment parameter and q is the inviscid external velocity.

RANS equations. RANS computation is used to investigate the aerodynamic characteristics of both the optimized airfoils and original airfoils. ANSYS ICEM CFD 16.0 is used as the mesh generator for all the cases. In the case of NACA0012, an airfoil study with angle of attack (AoA) ranging from 0° to 14° was conducted for validation and comparison with the experiments done by Lee and Gerontakos.[28] The simulated chord based Reynolds number is 1.35×10^5 with a turbulence intensity of 0.08%. A structured O grid with 200 nodes perpendicular to the airfoil surfaces and 500 nodes wrapped over each surface was applied to the two airfoils.

In the case of E387 as shown in Figure 4(a), a structured C-grid with 200 nodes perpendicular to the airfoil surfaces and 400 to 500 nodes wrapped over each surface was applied to both airfoils. Because of the circular TE of A7, an O-domain with a diameter of three chord lengths was used in the C-grid to wrap the airfoil, as presented in Figure 4(b). For different cases of AOA and Reynolds numbers, the LSB region has been refined with a minimum of 150 uniformly distributed points to capture the bubble characteristics in detail. To compare with McGhee et al.'s wind tunnel experiment,[27] three of the Reynolds numbers (1, 2, and 3×10^5) carried out in the experiment were selected for the RANS computation. The corresponding incoming turbulence intensities were 0.16%, 0.16%, and 0.2%, respectively.

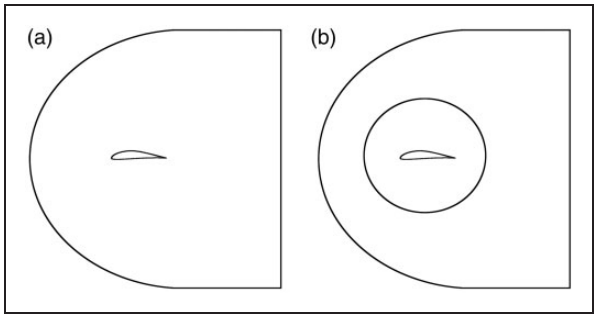

Figure 4. The schematic figure of the mesh domains of (a) E387 and (b) A7.

In both cases, the mesh was refined with twice the resolution in the streamwise and wall-normal directions from a coarse mesh, and it was determined to be an independent mesh when lift coefficient predictions showed negligible difference from a finer mesh but significant difference from a coarser mesh. The computational domain extends to 20 chord lengths in all directions for each airfoil, with a total number of approximately 200,000 grid cells and $y+ < 1.0$. The transition SST turbulence model which is based on the coupling of the k − ω SST transport equations with two other transport equations (in terms of the intermittency and momentum-thickness Reynolds number, respectively) has been selected as the eddy viscosity model in ANSYS Fluent 16.0.

Redesign of the LE of NACA0012

As one of the most common airfoils, NACA0012 is widely studied and applied.[34–36] The thickness distribution equation of NACA0012 is:

$$\begin{aligned} y/c = \pm 0.6[&0.2926\sqrt{x/c} - 0.126x/c \\ &- 0.3516(x/c)^2 + 0.2843(x/c)^3 \\ &- 0.1015(x/c)^4] \end{aligned} \quad (8)$$

The second-order derivative of this equation is infinite at the LE point and the surface curvature at this point is singular by the definition in equation (1). This is a typical curvature discontinuity, suitable for application of the CIRCLE method. Except the LE point, no curvature or slope-of-curvature discontinuity exists in the NACA0012 profile, because the second- and third-order derivatives of equation (8) are continuous. Consequently, only small improvement in aerodynamic performance can be achieved by fixing only one discontinuous point on the airfoil and keeping a nearly identical profile simultaneously. This case is used to illustrate the effects of curvature discontinuity on aerodynamic performance.

The design resulting from application of the CIRCLE method is shown in Figure 5, and this optimized airfoil is denoted as "QM13F." The newly

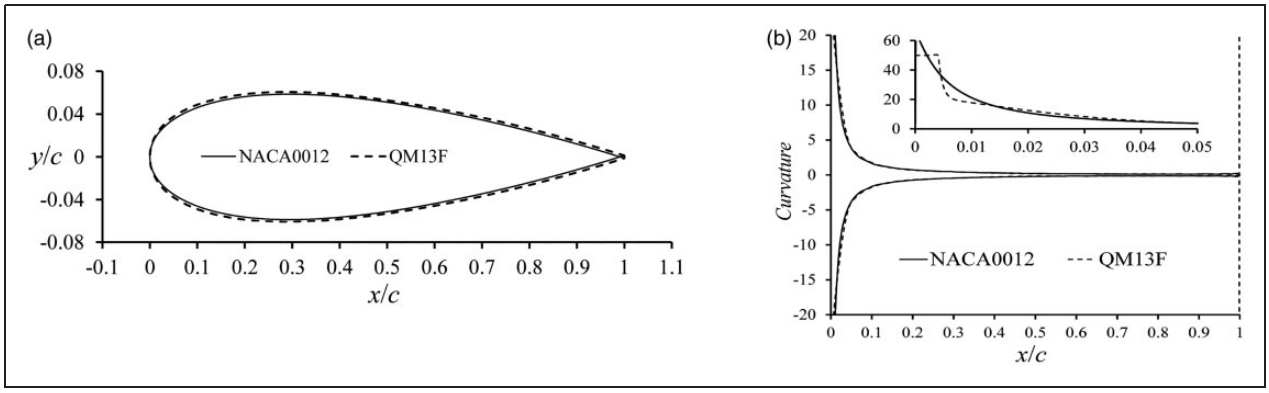

Figure 5. The comparison between (a) profiles and (b) surface curvature distributions of original airfoil NACA0012 and optimized airfoil QM13F. The small figure in (b) is a magnification in the LE area.

Table 1. Some key design parameters in the CIRCLE method.

TE radius	$\beta s2$ (°)	*Psm*	βsm (°)	$\beta s1$ (°)	LE radius	LE position
0.00145	79.5	(0.5, 0.0529)	−3.75	38	0.02	(0, 0)

designed airfoil profile deviates minimally from the original NACA0012, and some key parameters are shown in Table 1.

QM13F is also a symmetrical airfoil and has almost the same thickness distribution as the original airfoil. Since the CIRCLE method has been applied, the newly designed airfoil has a continuous surface and slope-of-surface distribution from TE to LE without the singularity at the LE point. The curvature distributions of the two airfoils are shown in Figure 5(b).

The lift coefficients (*Cl*) and drag coefficients (*Cd*) of the airfoils and experimental data of NACA0012 at Reynolds number 1.35×105 are presented in Figure 6. The RANS results of NACA0012 match well with the experimental data by Lee and Gerontakos.[28] The computation accurately predicts the stalling AoA and the corresponding *Cl* and *Cd*, although it slightly overestimates *Cl* values from 7° to 10° in Figure 6(a) and overestimates *Cd* values when the AoA is low, as shown in Figure 6(b). Both of these figures indicate that the two airfoils have the same lift and drag performance at this Reynolds number until the AoA reaches 10°. At the AoA > 10°, however, QM13F has a larger *Cl* and a reduced *Cd* compared with NACA0012. This numerical comparison between NACA0012 and QM13F indicates that the LE singularity of NACA0012 significantly improves the airfoils aerodynamic performance near the stalling AoA.

As shown in Figure 6, the main differences between the lift and drag performance of the two airfoils are shown at the AoA of approximately 13°. Therefore, the pressure coefficient (Cp) and skin friction coefficient (Cf) distributions of these airfoils at 13° are examined to further investigate the boundary layer behavior for different aerodynamic performance, as shown in Figure 7.

The difference in *Cp* distribution can be observed on the suction side near the LE region. In the magnified view in Figure 7(a), the RANS results of QM13F shows increased negative pressure over the LE suction side compared with the original NACA0012 due to the continuous surface curvature distribution, which results in better lift performance. The differences between the *Cf* distributions on the suction side are presented in Figure 7(b). This indicates that QM13F has a delayed separation point near the LE region because the *Cf* value of QM13F before the transition point is generally larger than that of NACA0012. QM13F provides reduced skin friction force without the LE curvature discontinuity as shown in Figure 7(b).

Both TATO and RANS methods are applied to NACA 0012 and QM13F at AoA = 13°, $\mathrm{Re} = 1.35 \times 10^5$ and the predictions are provided in Table 2. In the experimental work by Lee and Gerontakos,[28] the LSB on NACA 0012 at the same operating conditions appeared near the LE and the length is approximately 0.07 chord length (the bubble is too small to give an accurate length). Both numerical methods reproduced the bubble position and acceptably predicted the bubble length. TATO and RANS predicted that the length of the LSB on QM13F is 0.07 and 0.016 chord-length shorter than that on NACA 0012, resulting in better aerodynamic performance as shown in Figure 6.

It can be concluded that the removal of the LE surface curvature discontinuity results in higher lift and lower drag near stalling AoA due to the higher pressure differences between pressure and suction sides and delayed laminar separation.

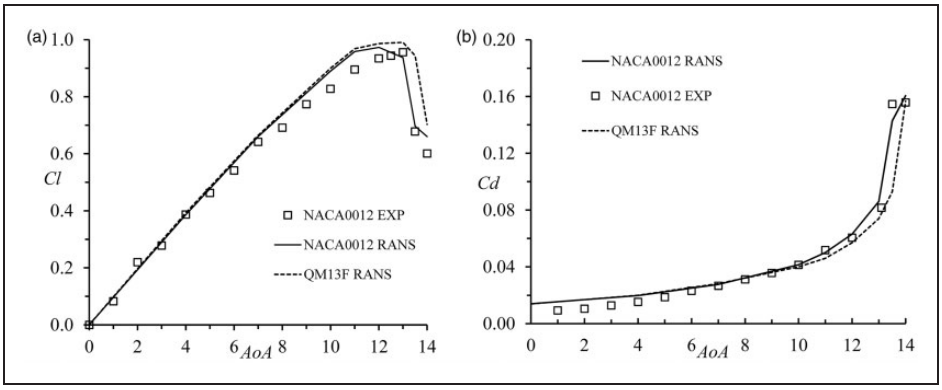

Figure 6. Comparison between (a) lift coefficients and (b) drag coefficients from RANS results and experimental work by Lee and Gerontakos.[28]

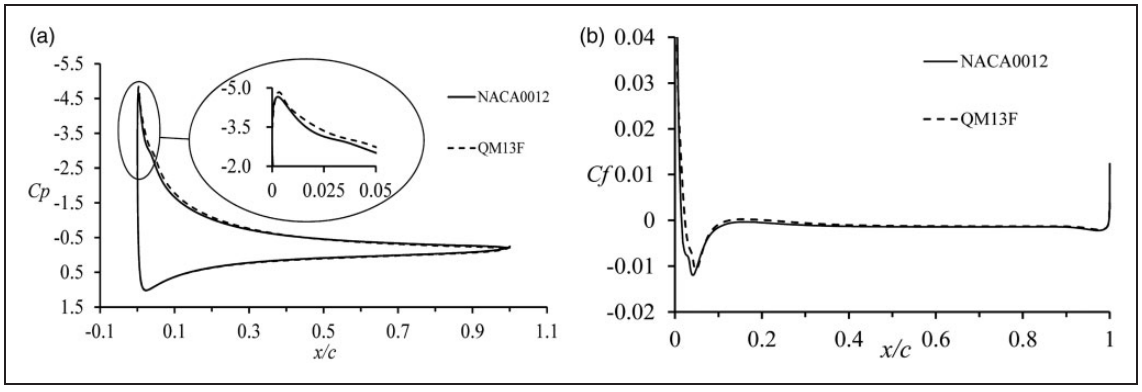

Figure 7. The RANS results comparison of (a) pressure coefficients and (b) upper surface skin friction coefficients at 13° angle of attack between NACA0012 and QM13F.

Table 2. The bubble length comparison between TATO and RANS for NACA 0012 and QM13F at $Re = 1.35 \times 10^5$, $AoA = 13°$.

	TATO			RANS		
	LS position	TR position	BL	LS position	TR position	BL
NACA0012	0.018	0.079	0.059	0.016	0.099	0.083
QM13F	0.024	0.076	0.052	0.025	0.092	0.067

LS: laminar separation; TR: turbulent re-attachment; BL: bubble length.

Redesign of the airfoil E387

Like many other airfoils, the original geometry of airfoil E387 exhibits slope-of-curvature discontinuities on its surface, observable at the region where the LE circle joins the airfoil surfaces among other places. The airfoil E387 is optimized by the CIRCLE method. The resulting airfoil A7 is presented and compared with the original airfoil. Figure 8(a) shows a comparison between the two airfoil geometries. A7 has a circular TE and E387 has a sharp TE, but the almost the same LE circle is present in both airfoils. A7 is slightly thicker than E387 from LE to TE, and A7 has mildly greater camber from LE to approximately 0.65 chord length and smaller camber for the rest of the chord length than E387. As indicated in Figure 8(b), E387 has slope-of-curvature discontinuities mainly on the suction surface, and an obvious "kink" is observable on each side of the airfoil E387. These slope-of-curvature discontinuities have been removed in the redesigned airfoil A7.

Lift and drag coefficients

It is a very straight forward way to compare airfoils performance by comparing their lift and drag coefficients. In this subsection, the simulated lift and drag coefficients of E387 and A7 are compared with show the aerodynamic performance improvement caused by removing slope-of-curvature discontinuities

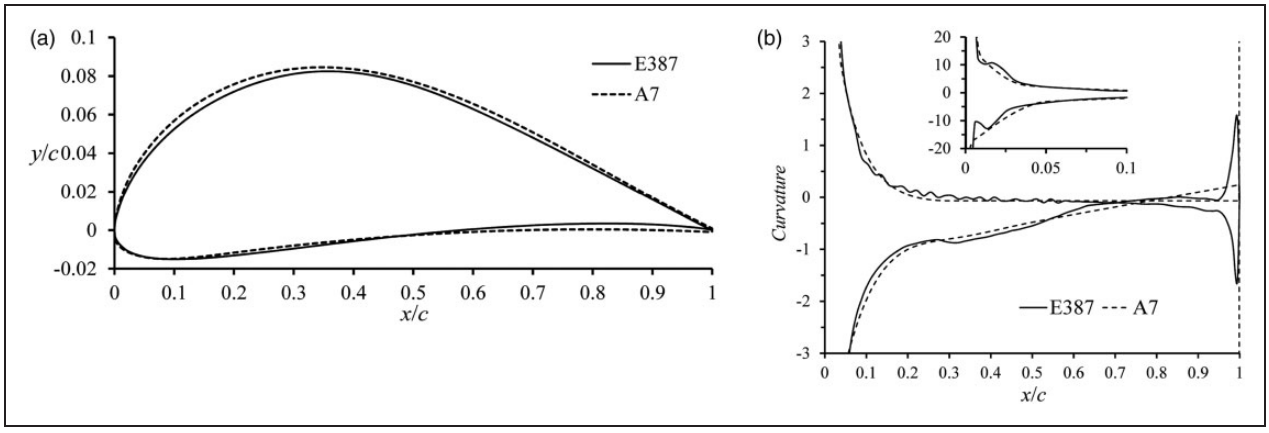

Figure 8. The comparison between (a) airfoil profiles and (b) curvature distributions of E387 and A7.

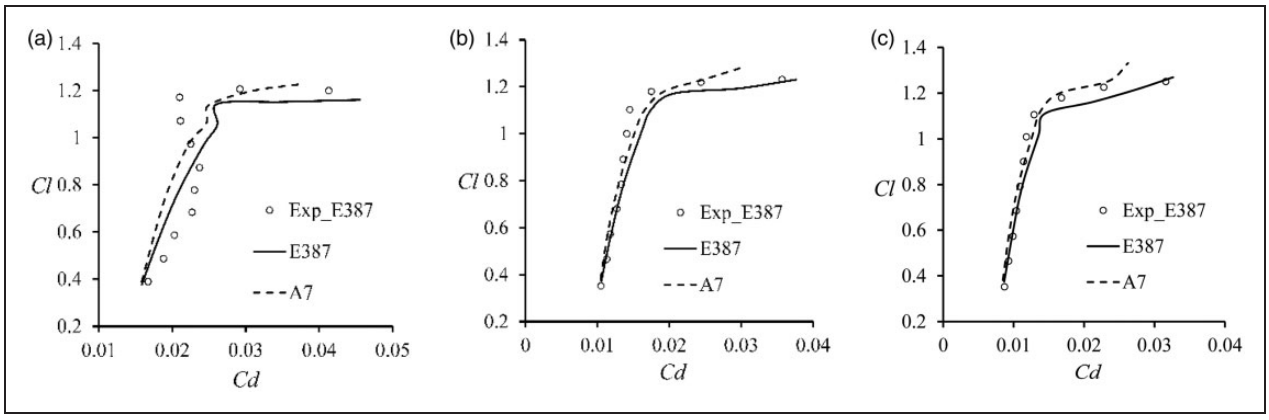

Figure 9. Comparison between lift-drag coefficients polar curves from RANS results and experimental work of E387 by McGhee et al.[27] at (a) $Re = 1 \times 10^5$, (b) $Re = 2 \times 10^5$, and (c) $Re = 3 \times 10^5$. The angles of attack of the experimental data range from 0° to 10°.

at Reynolds number 10^5, 2×10^5, and 3×10^5. The experiment carried out in the NASA Langley LTPT[27] is usually regarded as the benchmark to validate results of E387. This experiment has consequently been selected as the reference to validate the results from this article.

The *Cl*-*Cd* polar curves at three Reynolds numbers are shown in Figure 9(a) to (c). At all Reynolds numbers, the results of E387 RANS computation match well with the experimental data, and meanwhile the A7 RANS results shows improved *Cl* and *Cd* at all the AoA investigated as shown in Figure 9. These results also indicate that the higher the AoA, the better performance airfoil A7 can offer compared with E387.

It is worth to mention that the RANS predictions of Cl for E387 at $Re = 10^5$ are smaller than the experimental data when the AoA exceeds 8°, around which E387 experiences earlier transition to turbulence, while the improved A7 airfoil maintains the increasing trend of the *Cl*, as shown in Figure 9(a). The earlier laminar-turbulence transition of E387 causes a loss of lift as well as increased drag. The airfoil A7 has reduced *Cd* practically throughout the range of AoA.

Investigation of LSB

LSB dominates airfoil aerodynamic performance at low Reynolds numbers.[27] The details of the separation bubbles on both E387 and A7 are presented in this subsection to investigate the reasons for the improvements in aerodynamic performance. Figure 10(a) and (b) summarizes the separation points and re-attachment points of LSB at Reynolds number 1×10^5 and 2×10^5, respectively.

At $Re = 10^5$, TATO results provide good predictions of laminar separation positions while the RANS predictions starts to move rapidly toward the LE when the AoA is above 6°. This LE toward moving phenomenon causes larger separation bubble, resulting in lower *Cl* and higher *Cd* results than experimental data

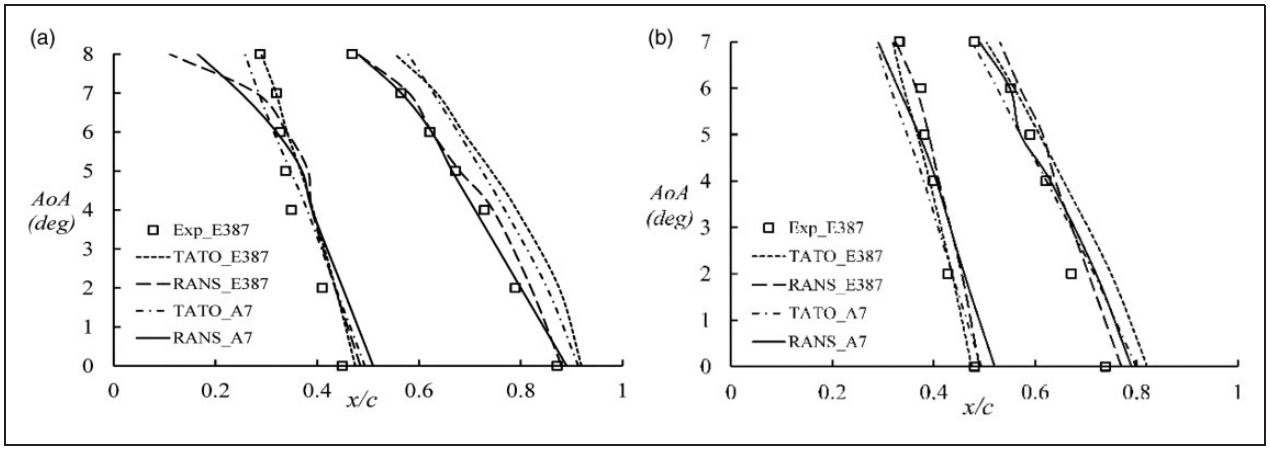

Figure 10. Separation and re-attachment points at $Re = 1 \times 10^5$ (a) and $Re = 2 \times 10^5$ (b).

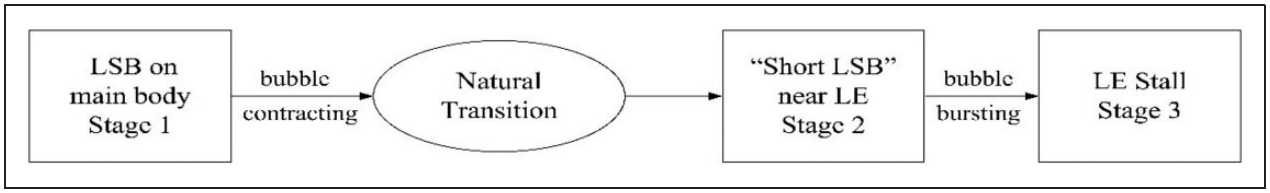

Figure 11. The growing and bursting process of LSB on an airfoil with increasing AoA at low Reynolds numbers. The predicted bubble lengths at Reynolds numbers 10^5 and 2×10^5 are summarized in Table 3. The prediction accuracy and computation time are also included in the table. At both Reynolds numbers in the table, the bubble length summarized from the experimental report[27] are acceptably reproduced in all cases except the 7° AoA. The TATO predictions provide more accurate results at $Re = 1 \times 10^5$ than at $Re = 2 \times 10^5$.

as previously shown in Figure 9(a). Meanwhile, RANS computations offer better predictions of turbulent re-attachment positions compared with TATO at $Re = 10^5$. At $Re = 2 \times 10^5$, both RANS and TATO methods provide acceptable results of laminar separation positions of E387 compared with the experimental data, while TATO slightly overestimates the re-attachment points when the AoA is low.

To analyze this table, it is essential to understand the growth and bursting process of LSB on E387 with increasing AoA at low Reynolds number as shown in Figure 11. In Horton's theory,[32] the process can be summarized as three stages. At a constant low Reynolds number, the LSB presents on the airfoil suction side at low angles of attack (Stage 1), and it moves toward the LE region and gets smaller with increasing AoA. When the AoA increases to a moderate value (e.g. E387 at 8° and $Re = 2 \times 10^5$ [27]), the laminar-turbulent transition occurs earlier than laminar separation ($x_{sep} > x_{tr}$ in Figure 1), and the airfoil experiences natural transition rather than LSB. When the AoA is higher than these transition angles, the LSB appears again at the LE region as a "short bubble" (Stage 2). The LSB bursts at the stalling AoA resulting in LE stall (Stage 3).

At the AoA of 7° in Table 3, the bubble lengths of E387 predicted by both RANS and TATO are more than 20% longer than those observed in the experiment. There are two possible explanations for this phenomenon. First, the sensitivity of the LSB at 7° has to be considered. The 7° AoA is close to the natural transition AoA as explained in the previous paragraph and the separation bubble appears to be sensitive and unstable. The sensitivity problem of the LSB at AoA around 7° has been observed by other researchers. Lin and Pauley[37] found that the freestream turbulence in the experiment may delay the separation and hence make a shorter bubble. They also found that the RANS computation overestimates the bubble length at the AoA of around 7°. Moreover, the inaccuracy of TATO calculations are mainly from the turbulent re-attachment predictions, which are calculated from equation (7). One possible reason for the delayed re-attachment predictions is that the classical re-attachment criterion does not take turbulence intensity of the experiment into consideration, which plays a key

role in the formation of the LSB, especially the location of the re-attachment point. Also, equation (7) is an empirical formula which is based on other experimental results, and it does not take the natural transition AOA of E387 or A7 into account. Consequently, longer bubbles at 7° are estimated by both computations.

The predicted bubble lengths of A7 are generally smaller than those of E387 except at the AoA of 7° at both Reynolds numbers. This can be explained by the growing and bursting process of an LSB in Figure 11. The bubble sizes of E387 have been efficiently reduced at 0° and 4° by removing the slope-of-curvature discontinuities. The redesigned airfoil A7 hence has better aerodynamic performance at low AoAs as shown in Figure 9. Compared with the LSBs on A7, the smaller bubbles of E387 at 7° indicate that the contraction speed of these bubbles become faster at 7° than at lower AoAs. They start moving rapidly toward the LE and getting into Stage 2 with increasing AoAs. However, as the AOA increases, the LSBs on the airfoil A7 contracts at the usual rate and stays in Stage 1. This phenomenon is more obvious at higher AoAs, which will be presented in the next subsection.

A comparison of the two approaches in terms of accuracy and computation time is presented in Table 3. Both methods offer acceptable results compared with the experimental data and RANS gives slightly better accuracy on bubble length prediction. However, the TATO method offers a much quicker response (within 5 s) and is hundreds of times quicker than RANS even if eight cores MPI are applied to the RANS computations. This makes TATO an affordable computing tool for rapid estimation of the LSB on an airfoil.

Table 3 also indicates that when the Reynolds number reaches 2×105, the curvature effects become less important for reducing the bubble size because the separation bubble is no longer the key factor affecting the airfoil performance. More specific details of the lift and drag force components are shown in Table 4.

While *Cl* is mostly dependent on the pressure forces acting on the airfoil as expected, there is also some effect due to the pressure and skin friction on the drag coefficient *Cd*. The continuous slope-of-curvature distribution not only increases the pressure component, which is the main source of the total *Cl*, but also increases the viscous component by 16.81%. The removal of the surface slope-of-curvature discontinuity from the upper surface leads to an obvious rise in pressure difference between the two surfaces and hence leads to an increased *Cl*. The continuous slope-of-curvature distribution also results in an 11.27% reduction of the pressure *Cd* and a 5.03% reduction of total *Cd*.

Cases of higher angles of attack

In "Lift and drag coefficients" section, RANS results indicated that the higher the AoA, the better

Table 3. Bubble length prediction accuracy and computation time comparison between RANS and TATO.

Airfoil		E387	A7	E387	A7	E387	A7	E387	A7	E387	A7	E387	A7
$Re \times 10^5$		1	1	1	1	1	1	2	2	2	2	2	2
AoA (°)		0	0	4	4	7	7	0	0	4	4	7	7
Bubble length (c)	Experiment	0.43	N/A	0.38	N/A	0.25	N/A	0.26	N/A	0.22	N/A	0.15	N/A
	TATO	0.444	0.419	0.401	0.388	0.316	0.332	0.316	0.305	0.254	0.242	0.188	0.190
	RANS	0.395	0.380	0.359	0.321	0.302	0.313	0.281	0.271	0.230	0.225	0.205	0.210
Error (%)	TATO	3.25	N/A	5.52	N/A	26.4	N/A	21.5	N/A	15.5	N/A	25.3	N/A
	RANS	−8.14	N/A	−5.53	N/A	20.8	N/A	8.08	N/A	4.55	N/A	36.67	N/A
Computation time (s)	TATO (1 core)	3.6	3.5	4.1	4.9	3.8	4.0	4.2	4.8	3.9	3.9	4.2	3.9
	RANS (8 cores)	2305	1735	1669	1352	1169	1563	1712	1533	2428	1666	1093	1111

The experimental data are from Mcghee et al.[27]

Table 4. The details of *Cl* and *Cd* components for E387 and A7 at $Re = 3 \times 10^5$, $AoA = 4°$.

	Cl			*Cd*		
	Pressure	Viscous	Total	Pressure	Viscous	Total
E387	8.037E-01	4.419E-04	8.042E-01	5.628E-03	5.699E-03	1.133E-02
A7	8.091E-01	5.162E-04	8.096E-01	4.994E-03	5.767E-03	1.076E-02

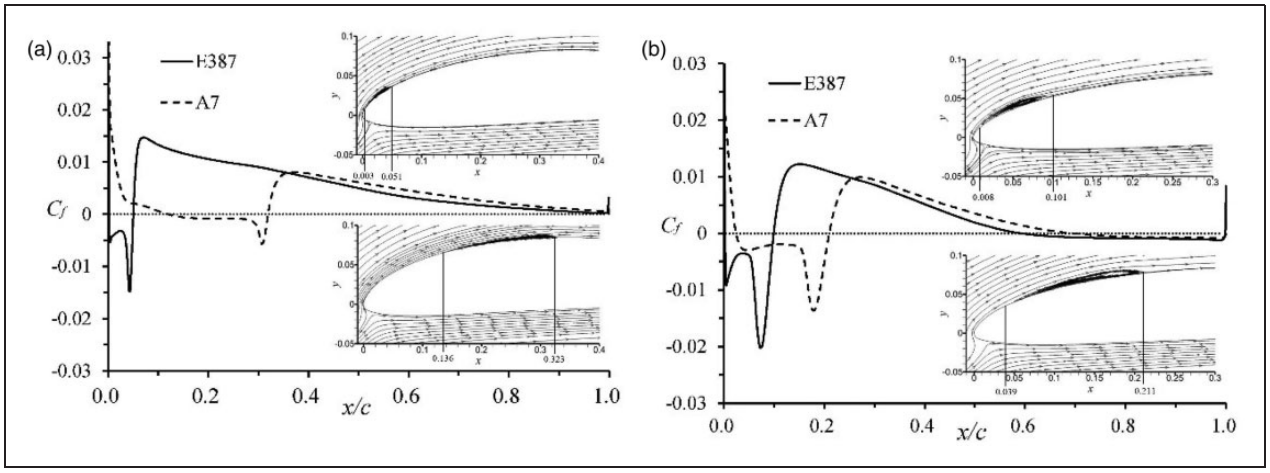

Figure 12. Comparison of skin friction coefficient distributions between E387 and A7 at (a) $Re = 3 \times 10^5$, $AoA = 8^\circ$, (b) $Re = 1 \times 10^5$, $AoA = 10^\circ$. The streamline figures are the streamline of E387 (top) and A7 (bottom), respectively, for the corresponding Re and AoA.

Table 5. The bubble length comparison between TATO and RANS at $Re = 1 \times 10^5$, $AoA = 10^\circ$.

		TATO			RANS		
		LS position	TR position	BL	LS position	TR position	BL
$Re = 1 \times 10^5$	E387	0.020	0.133	0.113	0.008	0.101	0.093
$AoA = 10^\circ$	A7	0.051	0.245	0.194	0.039	0.211	0.172

LS: laminar separation; TR: turbulent re-attachment; BL: bubble length.

performance the airfoil A7 can offer compared with E387. This subsection explains these observations by investigating the skin friction coefficient distributions and streamlines between E387 and A7. These are shown in Figure 12.

In Figure 12(a), E387 exhibits a short bubble at LE, making the airfoil experience earlier transition to turbulence at $Re = 3 \times 10^5$ and $AoA = 8^\circ$. With a turbulent re-attachment at the position $x/c = 0.051$, as shown in the streamline figure, the boundary layer becomes more energetic and hence significantly increases the skin friction force compared with airfoil A7. The continuous slope-of-curvature distribution results in a lower *Cf* distribution for the redesigned airfoil A7 with a LSB, which does not dominate the aerodynamic performance at $Re = 3 \times 10^5$.

As shown in Figure 11, the skin friction force generally increases from Stage 1 to 2 due to the more energetic turbulent boundary layer, and a bursting increase from Stage 2 to 3 due to the LE stall. This explains the difference in the LSB size in the case shown in Figure 12 and the case described previously in Table 3 at 7°. The RANS results indicate that discontinuous slope-of-curvature distributions make the LSB on E387 move into Stage 2 while the bubble on the airfoil A7 with an improved curvature distribution is still in Stage 1. This leads to an earlier laminar and turbulent separation, as well as an earlier transition process, and therefore higher *Cf*. The separation bubble on the airfoil A7 is caused only by the unavoidable adverse pressure gradient with no contribution from curvature discontinuity. Consequently, A7 has increased magnitudes of *Cl* and *Cd* performance (as the LSB is still in Stage 1) comparing with an earlier laminar and turbulent separation on the airfoil E387.

Both TATO and RANS methods are applied to Figure 12(b) to calculate bubble lengths and compared in Table 5. In the TATO method, equations (5) and (6) are used to calculate laminar separation position x_{sep} and transition position x_{tr} based on the inviscid external velocity from thin airfoil theory. As shown in Figure 1, equation (7) is used to calculate the re-attachment point when $x_{sep} < x_{tr}$. In the RANS method, the separation streamline and the airfoil surface are used to bound the bubble, and the coordinates from the separation point to the re-attachment point are obtained. Both methods predicted a short bubble near the LE of E387 and a longer bubble on the main body of A7.

The predictions are consistent with Horton's theory and the authors' inferences in last subsection. The continuous slope-of-curvature distribution delays the LSB's transition to move into Stage 2 and helps to control the LSB contraction speed when the AoA increases.

Figure 12(b) also shows at $\mathrm{Re} = 1 \times 10^5$ and $\mathrm{AoA} = 10^\circ$, the continuous slope-of-curvature distribution delayed the position of turbulence TE separation by more than 10% for the redesigned airfoil A7. As soon as the flow separates near the TE, the separated region merges with the wake and results in TE stall, causing lift loss and drag increase. Continuous slope-of-curvature distributions make the boundary layer flow attach to the airfoil surface for a longer surface distance and suppress the flow separation in the TE, and consequently improve airfoil performance.

Concluding remarks

This article presented a completed solution for profile design and aerodynamic performance computation methods for the airfoils with discontinuities in their curvature and slope-of-curvature distributions. A symmetrical airfoil NACA0012 and a non-symmetrical airfoil E387 were judiciously selected as examples of airfoils with surface curvature discontinuity and slope-of-curvature discontinuity, respectively. They were redesigned using the CIRCLE method to specifically investigate the effects of surface curvature on aerodynamic performance at different angles of attack and Reynolds numbers.

NACA0012 exhibits a surface curvature discontinuity at the LE stagnation point. The newly designed airfoil removed the LE singularity. RANS computational results indicated that the airfoil surface curvature discontinuity affects pressure and skin friction distribution, and hence affects lift and drag coefficients near the stalling AOA. The airfoil performance near the stalling angle is improved (an average 5% increase in lift and average 10% reduce in drag) by removing the curvature discontinuity.

E387 exhibits slope-of-curvature discontinuities in both surfaces. The newly designed airfoil deviates little in its profile geometry to the original airfoil but with no slope-of-curvature discontinuities. In this case, a rapid-response inviscid–viscid interaction scheme called TATO was introduced to compute the aerodynamic performance. The results are acceptable compared with the results from the RANS computations and experimental work. The TATO scheme provided much faster response than the RANS computation. The flow performance was analyzed for three different Reynolds numbers and it was shown that continuous slope-of-curvature distributions increased the lift coefficient and the reduced drag coefficient for all the Reynolds numbers studied. The separation bubble sizes were computed by RANS results, and compared well against available experimental data in the literature and an inviscid–viscid scheme of the second-order thin airfoil theory and boundary layer methods. For the cases at Reynolds numbers below 2×10^5 and relatively low angles of attack, the airfoil surface curvature affects the size of the LSB which dominates airfoil performance in these cases. The bubble sizes were successfully reduced by removing slope-of-curvature discontinuities, and the aerodynamic performance is consequently improved. For the cases at $\mathrm{Re} > 2 \times 10^5$, the factor that is important for the airfoil performance is no longer the separation bubble size but the inherent profile of the airfoil. At higher angles of attack for all cases, continuous slope-of-curvature distribution delayed LE separation, laminar-turbulence transition, and TE separation. Through these mechanisms, skin friction is reduced and improved aerodynamic performance is achieved.

It has been shown that airfoil surface curvature and slope-of-curvature distributions have significant effects on the boundary layer behavior. Continuous curvature and slope-of-curvature distributions provide better control of flow separation, inherently better profile drag and thereby improve Cl/Cd, leading to improving airfoil aerodynamic performance.

Acknowledgments

The authors acknowledge the contributions of MSc and PhD students, and postdocs, who over two decades have contributed to coding various aspects of the CIRCLE blade design method in FORTRAN, C++, and MATLAB, and on various platforms and operating systems.

Declaration of conflicting interests

The author(s) declared no potential conflicts of interest with respect to the research, authorship, and/or publication of this article.

Funding

The author(s) disclosed receipt of the following financial support for the research, authorship, and/or publication of this article: The PhD research of Xiang Shen is funded by China Scholarship Council (CSC)/Queen Mary Joint PhD scholarship.

References

1. Wortmann FX. A critical review of the physical aspects of airfoil design at low Mach numbers. *NASA CR* 2315: 179–196.
2. Ashrafizadeh A, Raithby GD and Stubley GD. Direct design of airfoil shape with a prescribed surface pressure. *Numerical Heat Transfer, Part B* 2004; 46: 505–527.

3. Hield P. Semi-inverse design applied to an eight stage transonic axial flow compressor. In: *ASME Turbo Expo 2008: Power for land, sea, and air,* Berlin, Germany, American Society of Mechanical Engineers, 9–13 June 2008, pp.293–303.
4. Birckelbaw L. Inverse airfoil design using the Navier-Stokes equations. AIAA paper, 1989, pp.89–2202.
5. Meauze G. Overview on blading design methods. AGARD Lecture Series 167, AGARD-LS-167, 1989.
6. Ives DC. A modern look at conformal mapping including multiply connected regions. *AIAA J* 1976; 14: 1006–1011.
7. Van Dyke MD. Second-order subsonic airfoil-section theory and its practical application. Technical Note 3390, National Advisory Committee for Aeronautics, Ames Aeronautical Laboratory, Moffett Field, CA, March 1955.
8. Hess JL. Panel methods in computational fluid dynamics. *Annu Rev Fluid Mech* 1990; 22: 255–274.
9. Almutairi JH, Jones LE and Sandham ND. Intermittent bursting of a laminar separation bubble on an airfoil. *AIAA J* 2010; 48: 414–426.
10. Pachidis V, Pilidis P, Talhouarn F, et al. A fully integrated approach to component zooming using computational fluid dynamics. *J Eng Gas Turb Power* 2006; 128: 579–584.
11. Korakianitis T. Prescribed-curvature-distribution airfoils for the preliminary geometric design of axial-turbomachinery cascades. *J Turbomach* 1993; 115: 325–333.
12. Hamakhan IA and Korakianitis T. Aerodynamic performance effects of leading-edge geometry in gas-turbine blades. *Appl Energy* 2010; 87: 1591–1601.
13. Song Y, Gu C-W and Xiao Y-B. Numerical and theoretical investigations concerning the continuous-surface-curvature effect in compressor blades. *Energies* 2014; 7: 8150–8177.
14. Korakianitis T. Design of airfoils and cascades of airfoils. *AIAA J* 1989; 27: 455–461.
15. Sommer L and Bestle D. Curvature driven two-dimensional multi-objective optimization of compressor blade sections. *Aerosp Sci Technol* 2011; 15: 334–342.
16. Siddappaji K, Turner MG and Merchant A. General capability of parametric 3d blade design tool for turbomachinery. In: *ASME Turbo Expo 2012: Turbine technical conference and Exposition*, Copenhagen, Denmark, American Society of Mechanical Engineers, 11–15 June 2012, pp.2331–2344.
17. Nemnem AF, Turner MG, Siddappaji K, et al. A smooth curvature-defined mean-line section option for a general turbomachinery geometry generator. In: *ASME Turbo Expo 2014: Turbine technical conference and exposition, V02BT39A026*, Düsseldorf, Germany, American Society of Mechanical Engineers, 16–20 June 2014.
18. Korakianitis T and Papagiannidis P. Surface-curvature-distribution effects on turbine-cascade performance. *J Turbomach* 1993; 115: 334–341.
19. Massardo A and Satta A. Axial flow compressor design optimization: Part I - Pitchline analysis and multivariable objective function influence. *J Turbomach* 1990; 112: 399–404.
20. Massardo A, Satta A and Marini M. Axial flow compressor design optimization: Part II - Through-flow analysis. *J Turbomach* 1990; 112: 405–410.
21. Song Y and Gu C. Effects of curvature continuity of compressor blade profiles on their performances. In: *ASME Turbo Expo 2014: Turbine technical conference and exposition, V02AT37A020*, Düsseldorf, Germany, American Society of Mechanical Engineers, 16–20 June 2014.
22. Korakianitis T, Rezaienia MA, Hamakhan IA, et al. Aerodynamic improvements of wind-turbine airfoil geometries with the prescribed surface curvature distribution blade design (CIRCLE) method. *J Eng Gas Turbines Power* 2012; 134: 082601.
23. Sandham ND. Transitional separation bubbles and unsteady aspects of aerofoil stall. *Aeronaut J* 2008; 112: 395–404.
24. Zhang MM, Wang GF and Xu JZ. Aerodynamic control of low-Reynolds-number airfoil with leading-edge protuberances. *AIAA J* 2013; 51: 1960–1971.
25. Korakianitis T, Rezaienia MA, Hamakhan IA, et al. Two- and three-dimensional prescribed surface curvature distribution blade design (CIRCLE) method for the design of high efficiency turbines, compressors, and isolated airfoils. *J Turbomach* 2013; 135: 041002.
26. Korakianitis T, Hamakhan IA, Rezaienia MA, et al. Design of high-efficiency turbomachinery blades for energy conversion devices with the three-dimensional prescribed surface curvature distribution blade design (CIRCLE) method. *Appl Energy* 2012; 89: 215–227.
27. Mcghee R, Walker B and Millard B. Experimental results for the Eppler 387 airfoil at low Reynolds numbers in the Langley low-turbulence pressure tunnel. Technical report, NASA, 1988.
28. Lee T and Gerontakos P. Investigation of flow over an oscillating airfoil. *J Fluid Mech* 2004; 512: 313–341.
29. Thwaites B. *Incompressible aerodynamics: an account of the theory and observation of the steady flow of incompressible fluid past aerofoils, wings*. New York: Clarendon Press, 1960.
30. Curle N and Skan SW. Approximate methods for predicting separation properties of laminar boundary layers. *Aeronaut Q* 1957; 8: 257–268.
31. Cebeci T and Bradshaw P. *Physical and computational aspects of convective heat transfer*. New York: Springer, 1988.
32. Horton HP. *Laminar separation bubbles in two and three dimensional incompressible flow*. PhD thesis, Queen Mary College, University of London, 1968.
33. Roberts WB. Calculation of laminar separation bubbles and their effect on airfoil performance. *AIAA J* 1980; 18: 25–31.
34. Sandberg RD, Jones LE and Sandham ND. Direct numerical simulations of forced and unforced separation bubbles on an airfoil at incidence. *J Fluid Mech* 2008; 602: 175–207.
35. Hansman RJ and Craig AP. Low Reynolds number tests of NACA 64-210, NACA 0012, and Wortmann FX67-K170 airfoils in rain. *J Aircraft* 1987; 24: 559–566.

36. Harris CD. Two-dimensional aerodynamic characteristics of the NACA 0012 airfoil in the Langley 8 foot transonic pressure tunnel. Technical report. Hampton, VA: NASA Langley Research Center, 1981.
37. Lin JCM and Pauley LL. Low-Reynolds-number separation on an airfoil. *AIAA J* 1996; 34: 1570–1577.

Appendix 1

Notation

$c_0, c_1, \ldots$	Coefficients in the segment $y3$ in the CIRCLE method
$C1s, C2s, \ldots$	Bezier control points (Figure 2(d))
C_d	drag coefficient, $C_d = D/(0.5\rho v^2 c)$, where D is the drag force, ρ is the air density, v is the freestream flow velocity, and c is the chord length of the airfoil
C_f	skin friction coefficient, $C_f = \tau_w/(0.5\rho v^2)$, where τ_w is the local wall shear stress
C_l	lift coefficient, $C_l = L/(0.5\rho v^2 c)$, where L is the lift force
C_p	pressure coefficient, $C_p = (p - p_\infty)/(0.5\rho v^2)$, where p is the local pressure, p_∞ is the freestream pressure
$Curv$	surface curvature
$Curv'$	slope of surface curvature
$k_1, k_2, \ldots$	exponential polynomials (equations (3) and (4))
m	separation parameter (equation (5))
P	points or nodes on the blade surfaces
q	external flow velocity (equations (5) and (7))
r	radius of curvature
Re	Reynolds number
(x, y)	Cartesian coordinates
$y1, y2, y3$	blade segments: leading edge, main part, and trailing edge (Figure 2)
β	blade-surface angle
θ	momentum thickness of boundary layer
Λ	re-attachment parameter (equation (7))
v	kinematic viscosity of air
$p1$	pressure side point (Figure 2)
$p2$	pressure side point (Figure 2)
pk	pressure side point (Figure 2)
pm	pressure side point (Figure 2)
$s1$	suction side point, $y3$ segment to LE circle (Figure 2)
$s2$	suction side point, TE circle to $y1$ segment (Figure 2)
sep	laminar separation
sk	suction side point, $y2$ to $y3$ segments (Figure 2)
sm	suction side point, $y1$ to $y2$ segments (Figure 2)
R	turbulent re-attachment (equation (7))
tr	laminar-turbulent transition